

A 10-node composite tetrahedral finite element for solid mechanics

J. T. Ostien^{1,*}, J. W. Foulk¹, A. Mota¹ and M. G. Veilleux²

¹*Mechanics of Materials Department, Sandia National Laboratories, Livermore, CA 94550, USA*

²*Multi-Physics Modeling and Simulation Department, Sandia National Laboratories, Livermore, CA 94550, USA*

SUMMARY

We propose a reformulation of the composite tetrahedral finite element first introduced by Thoutireddy *et al.* By choosing a different numerical integration scheme, we obtain an element that is more accurate than the one proposed in the original formulation. We also show that in the context of Lagrangian approaches, the gradient and projection operators derived from the element reformulation admit fully analytic expressions, which offer a significant improvement in terms of accuracy and computational expense. For plasticity applications, a mean-dilatation approach on top of the underlying Hu–Washizu variational principle proves effective for the representation of isochoric deformations. The performance of the reformulated element is demonstrated by hyperelastic and inelastic calculations. Copyright © 2016 John Wiley & Sons, Ltd.

Received 7 August 2015; Revised 16 December 2015; Accepted 11 January 2016

KEY WORDS: Hu–Washizu; tetrahedron; mixed formulation; plasticity

1. INTRODUCTION

Simplicial finite elements and specifically tetrahedral finite elements are well suited for meshing complex geometries such as curved bodies. In many cases, algorithms can automatically generate a quality tetrahedral mesh for non-trivial geometries, which does not hold, in general, for hexahedral meshes. Despite the decreased relative cost in generating tetrahedral discretizations, three dimensional Lagrangian finite element simulations, primarily used to model the behavior of solid bodies, have long depended on hexahedral meshing technology to achieve adequate levels of accuracy. Efforts at utilizing tetrahedral elements have proven difficult, in particular, for problems that involve isochoric plasticity, nearly incompressible materials, and significant bending [1–4]. For this reason, the exploration of tetrahedral finite elements that perform well in large deformation environments with inelastic constitutive models continues to be warranted.

Efforts towards the incorporation of simplicial technologies for solid mechanics applications include forays into stabilized methods [5–7], and novel nodal integration procedures [8–10], among other developments. An extensive discussion about different simplicial finite elements and their corresponding uses can be found in [1], particularly in the context of explicit transient solid dynamics codes. Scovazzi *et al.* [7] also consider the dynamic case and provide a substantial overview of the development of stabilized methods and comparison of their method with standard quadrilateral and hexahedral elements within the context of the B-bar operator formalism.

Herein, our purpose is to revisit, to extend the composite tetrahedral element formulation proposed in [4], based on [11], and to explore the performance of our extension in large deformation scenarios. In order to avoid ambiguity, the term composite finite element is used in this work in the same sense as [4]: a parent element is subdivided into smaller elements with separate interpolation functions for both types of elements. Other definitions for composite elements are also used elsewhere [12].

*Correspondence to: Jakob Ostien, Mechanics of Materials Department, Sandia National Laboratories, Livermore CA 94550, USA.

†E-mail: jstostie@sandia.gov

The formulation begins with the work of [4], who explicitly state the need for a tetrahedral finite element suitable for transient dynamics. In particular, the authors emphasize the suitability of this element because of the well-defined lumped mass and therefore improved behavior for applications in explicit transient dynamics and contact. The formulation is based on a 10-node tetrahedral finite element with a piecewise linear basis and assumed linear gradient space. Other B-bar-based formulations for tetrahedra have been proposed, such as ones that enforce the incompressibility constraint over a patch of elements [13].

As opposed to dynamics and contact, the present work focuses on improving the accuracy of the original formulation and evaluating the suitability for nearly incompressible response and large deformation plasticity. Although we choose to employ the same interpolation for the discretization of the Hu–Washizu variational principle, to address accuracy, we depart from the original formulation by introducing a different numerical integration scheme. One salient feature of our formulation is the separation of the reference configuration and the stress-free configuration. This allows the representation of the projection operators that arise from the proposed Hu–Washizu formulation in analytic form, thus by-passing the use of numerical integration for these operators. Additionally, to address element performance in the nearly incompressible limit and for isochoric motions, a volume-averaging procedure is examined for the volumetric response.

2. FINITE ELEMENT FORMULATION

Consider a body $B \subset \mathbb{R}^3$ undergoing a motion described by the mapping $x = \varphi(X, t) : B \times [t_1, t_2] \rightarrow \mathbb{R}^3$, with the deformation gradient defined by $F := \text{Grad } \varphi$.

Assume that the boundary ∂B , with unit normal N , is the union of a displacement boundary $\partial_\varphi B$ where boundary displacements $\chi : \partial_\varphi B \times [t_1, t_2] \rightarrow \mathbb{R}^3$ are prescribed, and a traction boundary $\partial_T B$ where tractions $T : \partial_T B \times [t_1, t_2] \rightarrow \mathbb{R}^3$ are applied ($\partial_\varphi B \cap \partial_T B = \emptyset$). Let also $RB : B \times [t_1, t_2] \rightarrow \mathbb{R}^3$ be the body force, with R the mass density in the reference configuration. Furthermore, for every $t \in [t_1, t_2]$, introduce the energy functional

$$\Phi_0[\varphi] := \int_B A(F) dV - \int_B RB \cdot \varphi dV - \int_{\partial_T B} T \cdot \varphi dS, \quad (1)$$

in which $A(F)$ is the Helmholtz free-energy density.

2.1. Hu–Washizu Functional

The energy (1) is modified by introducing a constraint to obtain the Hu–Washizu functional as [4]

$$\Phi[\varphi, \bar{F}, \bar{P}] := \int_B A(\bar{F}) dV + \int_B \bar{P} : (F - \bar{F}) dV - \int_B RB \cdot \varphi dV - \int_{\partial_T B} T \cdot \varphi dS, \quad (2)$$

in which \bar{F} is an additional deformation gradient field that is constrained to be equal to the kinematic deformation gradient F by means of the Lagrange multiplier \bar{P} . Although the Helmholtz free-energy density A is now evaluated using \bar{F} instead of F , the functionals (1) and (2) are equivalent at this stage because of this constraint.

Assume that $\varphi \in U := (W_2^1(B))^3$, $\bar{F}, \bar{P} \in V := (W_2^1(B))^{3 \times 3}$, in which $W_2^1(B)$ is the Sobolev space of square-integrable functions with square-integrable first derivatives. The functional (2) is optimized by applying variations with respect to the independent fields φ , \bar{F} , and \bar{P} . Define test functions corresponding to these fields as $\psi \in U$, $\eta, \zeta \in V$, with $\psi = \mathbf{0}$ on $\partial_\varphi B$. The variations follow as

$$\begin{aligned} D\Phi[\varphi, \bar{F}, \bar{P}](\psi) &= \int_B \bar{P} : \text{Grad} \psi dV - \int_B RB \cdot \psi dV - \int_{\partial_T B} T \cdot \psi dS = 0, \\ D\Phi[\varphi, \bar{F}, \bar{P}](\eta) &= \int_B (P - \bar{P}) : \eta dV = 0, \\ D\Phi[\varphi, \bar{F}, \bar{P}](\zeta) &= \int_B (F - \bar{F}) : \zeta dV = 0, \end{aligned} \quad (3)$$

where $P := \partial A / \partial \bar{F}$ is the first Piola–Kirchhoff stress. The corresponding Euler–Lagrange equations are as follows:

$$\begin{aligned} \operatorname{Div} \bar{P} + RB &= \mathbf{0} \quad \text{in } B, & \bar{P}N &= T \quad \text{on } \partial_T B, \\ \bar{P} &= P \quad \text{in } B, & \bar{F} &= F \quad \text{in } B, \end{aligned} \quad (4)$$

as expected.

2.2. Discretization

Henceforth, the fields $(\varphi, \bar{F}, \bar{P})$ and test functions (ψ, η, ζ) are considered discrete by introducing the discretizations as follows:

$$\begin{aligned} \varphi(X) &:= N_a(X)\varphi_a \in U_h, & \psi(X) &:= N_b(X)\psi_b \in U_h, \\ \bar{F}(X) &:= \lambda_\alpha(X)\bar{F}_\alpha \in V_h, & \eta(X) &:= \lambda_\beta(X)\eta_\beta \in V_h, \\ \bar{P}(X) &:= \lambda_\alpha(X)\bar{P}_\alpha \in V_h, & \zeta(X) &:= \lambda_\beta(X)\zeta_\beta \in V_h, \end{aligned} \quad (5)$$

where N_a and N_b are basis functions for φ and ψ and λ_α and λ_β are basis functions for (\bar{F}, \bar{P}) and (η, ζ) . $(a, b) \in [1 \dots N]$, and $(\alpha, \beta) \in [1 \dots M]$, in which N is the number of nodes for φ and M is the number of nodes for \bar{F} and \bar{P} , respectively. $U_h \subset U$ and $V_h \subset V$ are finite-dimensional subspaces of U and V , respectively. Introducing these discretizations into the variational statements (3) gives

$$\begin{aligned} D\Phi[\varphi, \bar{F}, \bar{P}](\psi) &= R_{\varphi;a}(\varphi) \cdot \psi_a = 0, \\ D\Phi[\varphi, \bar{F}, \bar{P}](\eta) &= R_{\bar{F};\alpha}(\bar{F}) \cdot \eta_\alpha = 0, \\ D\Phi[\varphi, \bar{F}, \bar{P}](\zeta) &= R_{\bar{P};\alpha}(\bar{P}) \cdot \zeta_\alpha = 0, \end{aligned} \quad (6)$$

together with the discrete statements of equilibrium as follows:

$$\begin{aligned} R_{\varphi;a}(\varphi) &:= \int_B \bar{P} \cdot \mathcal{B}_a \, dV - \int_B RB N_a \, dV - \int_{\partial_T B} T N_a \, dS = \mathbf{0}, \\ R_{\bar{F};\alpha}(\bar{F}) &:= \int_B \lambda_\alpha(P - \bar{P}) \, dV = \mathbf{0}, \\ R_{\bar{P};\alpha}(\bar{P}) &:= \int_B \lambda_\alpha(F - \bar{F}) \, dV = \mathbf{0} \end{aligned} \quad (7)$$

in which \mathcal{B}_a is a third-order tensor defined as follows:

$$\mathcal{B}_a(X) := \delta_{ik} \frac{\partial N_a(X)}{\partial X_J} e_i \otimes E_J \otimes e_k, \quad (8)$$

where orthonormal bases for the reference and current configurations are E_J and e_i , respectively, and which plays the role of the gradient operator such that

$$F(X) = \mathcal{B}_a(X)x_a. \quad (9)$$

In order to reduce the three-field Hu–Washizu formulation to a single field formulation, the basis functions λ_α are chosen as C^{-1} discontinuous across elements, and the fields \bar{F} and \bar{P} are determined at the element level by static condensation as follows:

$$\bar{P} = \lambda_\alpha \left(\int_\Omega \lambda_\alpha \lambda_\beta I \, dV \right)^{-1} \int_\Omega \lambda_\beta P \, dV, \quad (10)$$

$$\bar{F} = \lambda_\alpha \left(\int_\Omega \lambda_\alpha \lambda_\beta I \, dV \right)^{-1} \int_\Omega \lambda_\beta F \, dV, \quad (11)$$

in which Ω is the domain of a single element and I is the 3×3 identity. Note that λ_α and λ_β form a basis for the space V_h , therefore (10) and (11) are projections of the fields P and F onto V_h . It

follows then that the discrete statement of equilibrium (7) may be expressed at the element level as depending only on the discrete deformation mapping field φ as follows:

$$R_a(\varphi) := \int_{\Omega} \bar{P} \cdot \mathcal{B}_a dV - \int_{\Omega} RBN_a dV - \int_{\partial_T \Omega} TN_a dS = \mathbf{0}, \quad (12)$$

in which \bar{P} is given in (10). Note that \bar{F} as given in (11) also enters this expression as it is needed to compute P .

2.3. Linearization

To obtain solutions for the nonlinear discrete variational statement (12), one may apply Newton-type methods or other related linearization-based techniques so that incremental solutions can be obtained from the directional derivative of the residual at each incremental step. Assuming that all loads are conservative, the linear approximation of the residual at the element level for φ is as follows:

$$R_a(\varphi_{n+1}) \approx R_a(\varphi_n) + DR_a[\varphi_n](\Delta\varphi), \quad (13)$$

where $\Delta\varphi$ denotes the linear increment from φ_n to φ_{n+1} . Introducing the discretization (5) for the increments and after some lengthy but straightforward algebraic manipulation, the directional derivative with respect to φ_n yields

$$DR_a[\varphi_n](\Delta\varphi) = K_{ab} \cdot \Delta\varphi_b \quad (14)$$

where

$$K_{ab} := \int_{\Omega} \bar{\mathcal{B}}_a^T : \mathbb{C} : \bar{\mathcal{B}}_b dV, \quad \mathbb{C}(\bar{F}) := \frac{\partial^2 A(\bar{F})}{\partial \bar{F} \partial \bar{F}}, \quad (15)$$

and the B-bar gradient operator

$$\bar{\mathcal{B}}_a(X) := \lambda_\alpha(X) \left[\int_{\Omega} \delta_{ik} \lambda_\alpha(X) \lambda_\beta(X) dV \right]^{-1} \int_{\Omega} \lambda_\beta(X) \frac{\partial N_a(X)}{\partial X_J} dV e_i \otimes E_J \otimes e_k. \quad (16)$$

We elaborate upon the significance and simplification that can be introduced into this operator in the next section. Note also that with these definitions, (12) also admits the equivalent representation now in terms of the B-bar gradient operator as follows:

$$R_a(\varphi) := \int_{\Omega} P \cdot \bar{\mathcal{B}}_a dV - \int_{\Omega} RBN_a dV - \int_{\partial_T \Omega} TN_a dS = \mathbf{0}. \quad (17)$$

3. ELEMENT DEFINITION

Following [4], we choose a simplicial topology for the finite elements that define the basis functions in (5). In particular, the composite tetrahedral element can be viewed as consisting of 12 four-node linear tetrahedral elements, referred to as sub-tetrahedra, as shown in Figure 1. The interpolation for the deformation mapping φ is chosen as C^0 piecewise linear, that is, linear in each sub-tetrahedron. The assumed deformation gradient \bar{F} and first Piola–Kirchhoff stress \bar{P} fields, however, are interpolated by C^{-1} linear functions that are defined over the entire parent element and are discontinuous between parent elements, which result in well-defined lumped masses and reduce the number of volume constraints. We show in Section 4, however, that this reduction in volume constraints is insufficient to prevent locking in nearly incompressible or fully isochoric deformations. We mitigate the locking phenomenon by recourse to a mean-dilatation or volume-average method described in Section 3.4.

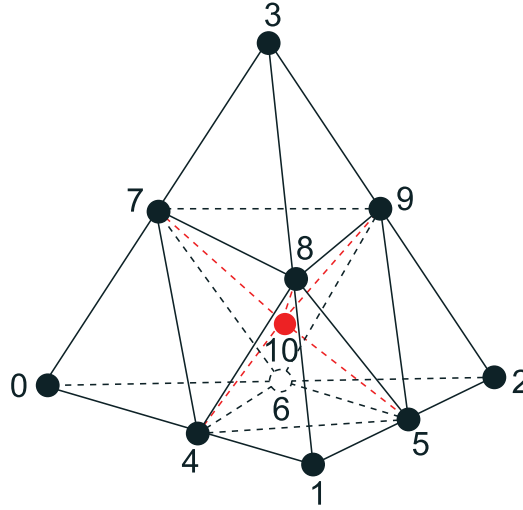


Figure 1. Geometry and node numbering for the composite tetrahedron.

As with the original formulation, the 12 sub-tetrahedra are constructed by defining an auxiliary node that is placed at the average location of the six edge nodes. This ensures symmetry of the sub-tetrahedra in the reference configuration. For a single element, the reference position of the auxiliary node is as follows:

$$X_{10} := \frac{1}{6} \sum_{i=4}^9 X_i. \quad (18)$$

Similarly, in the deformed configuration, the position of the auxiliary node is defined as follows:

$$x_{10} := \frac{1}{6} \sum_{i=4}^9 x_i. \quad (19)$$

Note that the edge nodes need not be aligned with the corner nodes in the general case. Nevertheless, requiring this in the reference configuration leads to significant improvements in the computational performance of the element, as it will be shown in Section 3.2. In particular, the discrete projection operators defined in (10) and (11) admit fully analytic expressions that can be pre-computed once and for all.

3.1. Parametric domains and shape functions

The sub-tetrahedra in Figure 1 are defined in Table I in terms of the parametric coordinates ξ_1 , ξ_2 , and ξ_3 of the parent tetrahedron, where we have also introduced the definition $\xi_0 := 1 - \xi_1 - \xi_2 - \xi_3$ for convenience.

The connectivity of the 12 sub-tetrahedra is shown in Table II, which also allows for a simple inverse mapping to determine which sub-tetrahedra are attached to a specific node. These sub-tetrahedra play an important role in the definition of the shape functions, as the latter change depending on the location of the point of evaluation. This is clearly illustrated in (20) below.

Next, we show the shape functions for the 10 nodes and the auxiliary node in terms of the parametric coordinates. We previously used N_a for basis functions written in terms of physical coordinates, for example, (5), but with a slight abuse of notation, we keep this convention and also employ N_a for shape functions written in parametric coordinates. Let us also define $\xi := (\xi_1, \xi_2, \xi_3)$. The first four nodes are connected to only one sub-tetrahedron each, and therefore, this permits the definition

Table I. Parametric domains for the 12 sub-tetrahedra.

Sub-tetrahedron	$\xi_i \in [a, b]$			
	ξ_0	ξ_1	ξ_2	ξ_3
E_0	$\frac{1}{2}, 1$	$0, 1$	$0, 1$	$0, 1$
E_1	$0, 1$	$\frac{1}{2}, 1$	$0, 1$	$0, 1$
E_2	$0, 1$	$0, 1$	$\frac{1}{2}, 1$	$0, 1$
E_3	$0, 1$	$0, 1$	$0, 1$	$\frac{1}{2}, 1$
E_4	$0, \frac{1}{2}$	$\frac{1}{4}, \frac{1}{2}$	$0, \frac{1}{2}$	$0, \frac{1}{2}$
E_5	$0, \frac{1}{2}$	$0, \frac{1}{2}$	$\frac{1}{4}, \frac{1}{2}$	$0, \frac{1}{2}$
E_6	$0, \frac{1}{2}$	$0, \frac{1}{2}$	$0, \frac{1}{2}$	$\frac{1}{4}, \frac{1}{2}$
E_7	$\frac{1}{4}, \frac{1}{2}$	$\frac{1}{4}, \frac{1}{2}$	$0, \frac{1}{4}$	$\frac{1}{4}, \frac{1}{2}$
E_8	$\frac{1}{4}, \frac{1}{2}$	$\frac{1}{4}, \frac{1}{2}$	$\frac{1}{4}, \frac{1}{2}$	$0, \frac{1}{4}$
E_9	$0, \frac{1}{4}$	$\frac{1}{4}, \frac{1}{2}$	$\frac{1}{4}, \frac{1}{2}$	$\frac{1}{4}, \frac{1}{2}$
E_{10}	$\frac{1}{4}, \frac{1}{2}$	$0, \frac{1}{4}$	$\frac{1}{4}, \frac{1}{2}$	$\frac{1}{4}, \frac{1}{2}$
E_{11}	$\frac{1}{4}, \frac{1}{2}$	$0, \frac{1}{2}$	$0, \frac{1}{2}$	$0, \frac{1}{2}$

Table II. Connectivity for the 12 sub-tetrahedra.

Sub-tetrahedron	Nodes			
E_0	0	4	6	7
E_1	1	5	4	8
E_2	2	6	5	9
E_3	3	8	7	9
E_4	4	8	5	10
E_5	5	8	9	10
E_6	9	8	7	10
E_7	7	8	4	10
E_8	4	5	6	10
E_9	5	9	6	10
E_{10}	9	7	6	10
E_{11}	7	4	6	10

of the shape functions in terms of a single sub-tetrahedron as follows:

$$\begin{aligned}
 N_0(\xi) &:= \begin{cases} 2\xi_0 - 1, & \text{if } \xi_0 \in [\frac{1}{2}, 1]; \\ 0, & \text{if } \xi_0 \in [0, \frac{1}{2}]; \end{cases} & N_1(\xi) &:= \begin{cases} 2\xi_1 - 1, & \text{if } \xi_1 \in [\frac{1}{2}, 1]; \\ 0, & \text{if } \xi_1 \in [0, \frac{1}{2}]; \end{cases} \\
 N_2(\xi) &:= \begin{cases} 2\xi_2 - 1, & \text{if } \xi_2 \in [\frac{1}{2}, 1]; \\ 0, & \text{if } \xi_2 \in [0, \frac{1}{2}]; \end{cases} & N_3(\xi) &:= \begin{cases} 2\xi_3 - 1, & \text{if } \xi_3 \in [\frac{1}{2}, 1]; \\ 0, & \text{if } \xi_3 \in [0, \frac{1}{2}]; \end{cases}
 \end{aligned} \tag{20}$$

Each of the edge nodes four to nine is connected to six sub-tetrahedra, and therefore, their corresponding shape functions are defined piecewise. Upon inspection, further simplification arises from the recognition that typically the same shape function is defined over four of the sub-tetrahedra as follows:

$$\begin{aligned}
N_4(\xi) &:= \begin{cases} 2\xi_1, & \text{if } \xi_0 \in [\frac{1}{2}, 1]; \\ 2\xi_0, & \text{if } \xi_1 \in [\frac{1}{2}, 1]; \\ 2\xi_{01} - 1, & \text{if } \xi_{01} \in [\frac{1}{2}, 1]; \\ 0, & \text{if } \xi_{01} \in [0, \frac{1}{2}]; \end{cases} & N_5(\xi) &:= \begin{cases} 2\xi_2, & \text{if } \xi_1 \in [\frac{1}{2}, 1]; \\ 2\xi_1, & \text{if } \xi_2 \in [\frac{1}{2}, 1]; \\ 2\xi_{12} - 1, & \text{if } \xi_{12} \in [\frac{1}{2}, 1]; \\ 0, & \text{if } \xi_{12} \in [0, \frac{1}{2}]; \end{cases} \\
N_6(\xi) &:= \begin{cases} 2\xi_2, & \text{if } \xi_0 \in [\frac{1}{2}, 1]; \\ 2\xi_0, & \text{if } \xi_2 \in [\frac{1}{2}, 1]; \\ 2\xi_{02} - 1, & \text{if } \xi_{02} \in [\frac{1}{2}, 1]; \\ 0, & \text{if } \xi_{02} \in [0, \frac{1}{2}]; \end{cases} & N_7(\xi) &:= \begin{cases} 2\xi_3, & \text{if } \xi_0 \in [\frac{1}{2}, 1]; \\ 2\xi_0, & \text{if } \xi_3 \in [\frac{1}{2}, 1]; \\ 2\xi_{03} - 1, & \text{if } \xi_{03} \in [\frac{1}{2}, 1]; \\ 0, & \text{if } \xi_{03} \in [0, \frac{1}{2}]; \end{cases} \\
N_8(\xi) &:= \begin{cases} 2\xi_3, & \text{if } \xi_1 \in [\frac{1}{2}, 1]; \\ 2\xi_1, & \text{if } \xi_3 \in [\frac{1}{2}, 1]; \\ 2\xi_{13} - 1, & \text{if } \xi_{13} \in [\frac{1}{2}, 1]; \\ 0, & \text{if } \xi_{13} \in [0, \frac{1}{2}]; \end{cases} & N_9(\xi) &:= \begin{cases} 2\xi_3, & \text{if } \xi_2 \in [\frac{1}{2}, 1]; \\ 2\xi_2, & \text{if } \xi_3 \in [\frac{1}{2}, 1]; \\ 2\xi_{23} - 1, & \text{if } \xi_{23} \in [\frac{1}{2}, 1]; \\ 0, & \text{if } \xi_{23} \in [0, \frac{1}{2}]; \end{cases}
\end{aligned} \tag{21}$$

where $\xi_{pq} := \xi_p + \xi_q$. The auxiliary node 10 is connected to the eight interior sub-tetrahedra; therefore, its corresponding shape function is defined as follows:

$$N_{10}(\xi) := \begin{cases} 2 - 4\xi_1, & \text{if } \xi \in E_4; \\ 4\xi_0, & \text{if } \xi \in E_5; \\ 2 - 4\xi_3, & \text{if } \xi \in E_6; \\ 4\xi_2, & \text{if } \xi \in E_7; \\ 4\xi_3, & \text{if } \xi \in E_8; \\ 2 - 4\xi_2, & \text{if } \xi \in E_9; \\ 4\xi_1, & \text{if } \xi \in E_{10}; \\ 2 - 4\xi_0, & \text{if } \xi \in E_{11}. \end{cases} \tag{22}$$

Employing these shape functions, the deformed configuration within an element, for instance, may be expressed as follows:

$$x(\xi) = \sum_{a=0}^{10} N_a(\xi) x_a. \tag{23}$$

The auxiliary node 10 exists merely for convenience: it does not carry any associated degrees of freedom and therefore does not enter the system of equations. Thus, effective shape functions for the mid-side nodes four to nine in which node 10 is eliminated may be defined by substituting (19) into (23) by effectively distributing the contributions of (22) to N_4, \dots, N_9 . Once more, rather than establish another notation for the shape functions, we will adhere henceforth to the convention that summations on N_a will span from 0, \dots , 9 and that N_4, \dots, N_9 will now contain the contributions from N_{10} .

3.2. Gradient operator

The edge nodes need not be colinear with the corner nodes in general. It is shown in this section, however, that requiring that the edge nodes be the midpoints of the edges in the reference configuration leads to significant simplification in the construction of the gradient operator. In particular, it will be shown here that this requirement results in fully analytic expressions for the gradient operator and thus this operator may be pre-computed at the beginning of a calculation once and for all. Again, with a slight abuse of notation, we use the same symbols for functions with respect to physical or parametric coordinates and let the argument X or ξ denote which one is used in a specific context.

Using standard isoparametric arguments and the chain rule, the derivatives of the shape functions with respect to the reference configuration may be written as follows:

$$\frac{\partial N_a(X)}{\partial X} = \frac{\partial N_a(\xi)}{\partial \xi} \frac{\partial \xi(X)}{\partial X} \quad (24)$$

for each element. It follows then that

$$\frac{\partial N_a(X)}{\partial X} = \frac{\partial N_a(\xi)}{\partial \xi} \left[\frac{\partial \xi(X)}{\partial X} \right]^{-1}. \quad (25)$$

To obtain derivatives with respect to physical coordinates, one needs only to define the gradient operator with respect to the parametric coordinates. For this particular element formulation, $\frac{\partial N_a(\xi)}{\partial \xi}$ in (25) will be piecewise constant across the 12 linear sub-tetrahedra. More importantly, those piecewise constant derivatives will be projected onto the linear space spanned by $\lambda_\alpha(X)$. By analogy to the gradient operator $\bar{\mathcal{B}}_a$ defined in (8) and (9), we re-express (11) for a single element Ω through a projected gradient operator $\bar{\mathcal{B}}_a$ as follows:

$$\bar{F}(X) := \bar{\mathcal{B}}_a(X) x_a \quad (26)$$

where

$$\bar{\mathcal{B}}_a(X) := \lambda_\alpha(X) \left[\int_{\Omega} \delta_{ik} \lambda_\alpha(X) \lambda_\beta(X) dV \right]^{-1} \int_{\Omega} \lambda_\beta(X) \frac{\partial N_a(X)}{\partial X_J} dV e_i \otimes E_J \otimes e_k. \quad (27)$$

3.2.1. Simplified parametric operator. To enable analytic expressions, we now deviate from prior work and define the gradient operator in terms of the parent element Ω_ξ in parametric coordinates ξ with an orthonormal basis a_l . We begin with (27) and find

$$\bar{\mathcal{B}}_a(\xi) := \lambda_\alpha(\xi) \left[\int_{\Omega_\xi} \delta_{ik} \lambda_\alpha(\xi) \lambda_\beta(\xi) J_\xi dV_\xi \right]^{-1} \int_{\Omega_\xi} \lambda_\beta(\xi) \frac{\partial N_a(\xi)}{\partial \xi} \frac{\partial \xi(X)}{\partial X_J} J_\xi dV_\xi e_i \otimes E_J \otimes e_k. \quad (28)$$

Note that this operator still yields the discrete deformation gradient but now evaluated at parametric coordinates, that is, $\bar{F}(\xi) = \bar{\mathcal{B}}_a(\xi) x_a$. We remark that if the edge nodes (4, 5, 6, 7, 8, 9) are constructed to be the midpoints between corner nodes (0, 1, 2, 3), the integration of (28) can be simplified. The derivative $\frac{\partial \xi(X)}{\partial \xi}$, its inverse $\frac{\partial \xi(X)}{\partial X}$, and J_ξ are constant as $X(\xi)$ is continuous and varies linearly with ξ . Thus, the term $\frac{\partial \xi(X)}{\partial X}$ can be factored out of the volume integral, and the corresponding determinants J_ξ will reduce to the identity. The new expression for the gradient operator is as follows:

$$\bar{\mathcal{B}}_a(\xi) = \lambda_\alpha(\xi) \left[\int_{\Omega_\xi} \delta_{ik} \lambda_\alpha(\xi) \lambda_\beta(\xi) dV_\xi \right]^{-1} \int_{\Omega_\xi} \lambda_\beta(\xi) \frac{\partial N_a(\xi)}{\partial \xi} dV_\xi \left(\frac{\partial \xi}{\partial X_J} \right) e_i \otimes E_J \otimes e_k, \quad (29)$$

which can be further simplified through the introduction of a new gradient operator with respect to the parametric coordinates

$$\bar{\mathcal{B}}_a(\xi) = \bar{\mathcal{L}}_{a;ilk}(\xi) \left(\frac{\partial \xi_l}{\partial X_J} \right) e_i \otimes E_J \otimes e_k \quad (30)$$

where

$$\bar{\mathcal{L}}_a(\xi) := \lambda_\alpha(\xi) \delta_{ik} (M_{\alpha\beta})^{-1} \int_{\Omega_\xi} \lambda_\beta(\xi) \frac{\partial N_a(\xi)}{\partial \xi_l} dV_\xi e_i \otimes a_l \otimes e_k \quad (31)$$

and

$$M_{\alpha\beta} := \int_{\Omega_\xi} \lambda_\alpha(\xi) \lambda_\beta(\xi) dV_\xi. \quad (32)$$

The operator $\bar{\mathcal{L}}_a(\xi)$ may be interpreted as a gradient operator with respect to the parametric domain. In addition, (32) can be integrated analytically, and the exact expression is shown in Appendix 6. Seeking further simplification, we can re-express the integral in (31) over the sub-tetrahedra E_S given the fact that the derivatives $\frac{\partial N_a(\xi)}{\partial \xi}$ are piecewise constant as follows:

$$\bar{\mathcal{L}}_a(\xi) = \lambda_\alpha(\xi) \delta_{ik} (M_{\alpha\beta})^{-1} \sum_{S=0}^{11} \frac{\partial N_a}{\partial \xi_l} \int_{E_S} \lambda_\beta(\xi) dV_\xi e_i \otimes a_l \otimes e_k. \quad (33)$$

The remaining integral in (33), which only contains the shape functions of the parent tetrahedron $\lambda_\beta(\xi)$, can be evaluated analytically over each sub-tetrahedra E_S . Integrating, summing, projecting via $(M_{\alpha\beta})^{-1}$, and interpolating, we can obtain an analytic operator as a function of ξ_0, ξ_1, ξ_2 , and ξ_3 . The remarkably simple analytic form for $\bar{\mathcal{L}}_a(\xi)$ is given in Appendix 6.

Again, we note that $\frac{\partial X}{\partial \xi}$ is constant for tetrahedra with edge nodes that are midpoints of the corner nodes. By also noting that $\bar{\mathcal{L}}_a(\xi)$ is a gradient operator that has the ability to recover a uniform gradient, we can write

$$\frac{\partial X}{\partial \xi} \equiv \bar{\mathcal{L}}_a(\xi) X_a. \quad (34)$$

This allows for a further modification in the computation of the discrete deformation gradient in (26) that proves extremely useful in computer implementation as follows:

$$\bar{F}(\xi) = \bar{\mathcal{L}}_a(\xi) x_a [\bar{\mathcal{L}}_b(\xi) X_b]^{-1} \quad (35)$$

and thus

$$\bar{\mathcal{B}}_a(\xi) = \bar{\mathcal{L}}_{a;ilk}(\xi) [\bar{\mathcal{L}}_{b;JlM}(\xi) X_{b;M}]^{-1} e_i \otimes E_J \otimes e_k. \quad (36)$$

This modification provides two advantages: (1) the deformation gradient $\bar{F}(\xi)$ can now be computed by applying the same simple analytic operator $\bar{\mathcal{L}}_a(\xi)$ to both reference and deformed nodal coordinates; and (2) the global operator $\bar{\mathcal{B}}_a(\xi)$ is expressed in parametric coordinates; therefore, we can merely evaluate and store it at each integration point for the entirety of the calculation.

3.3. Projection operators

In addition to developing gradient operators to obtain the discrete deformation gradient noted in (11), we also develop projection operators for the efficient evaluation of (10). The development is straightforward. In Section 3.2, we derived gradient operators $\bar{\mathcal{B}}_a$ and $\bar{\mathcal{L}}_a$ that act on nodal values. In this section, we will introduce an operator that in its final form acts on field values of the stress or deformation gradient at integration points. Although one could develop operators for any cubature, we restrict development to the standard Gauss–Legendre four-point and five-point integration schemes. We first re-express (10) for a single element Ω in parametric coordinates as follows:

$$\bar{P}(\xi) = \lambda_\alpha(\xi) \left(\int_{\Omega_\xi} \delta_{ik} \lambda_\alpha(\xi) \lambda_\beta(\xi) J_\xi dV_\xi \right)^{-1} \int_{\Omega_\xi} \lambda_\beta(\xi) P(\xi) J_\xi dV_\xi e_i \otimes e_k. \quad (37)$$

Employing the simplifications noted in Section 3.2, we obtain

$$\bar{P}(\xi) = \lambda_\alpha(\xi) \delta_{ik} (M_{\alpha\beta})^{-1} \int_{\Omega_\xi} \lambda_\beta(\xi) P(\xi) dV_\xi e_i \otimes e_k. \quad (38)$$

Although the first Piola–Kirchhoff stress $P(\xi)$ in the integrand of (38) is expressed as a function of ξ , we only calculate and store $P(\xi)$ at the integration points. We term the first Piola–Kirchhoff stress at integration point g to be $P_g(\xi_g)$. Given the integration points for a cubature rule, we can calculate $\bar{P}(\xi)$ through substitution, summation, and evaluation. For simplicity, we define the parametric projection operator to be

$$\bar{P}(\xi) := \bar{Q}_g(\xi) P_g \quad (39)$$

and remind the reader that g sums over the number of integration points. Projection operators for the four-point and five-point rules are $\bar{Q}_g^4(\xi)$ and $\bar{Q}_g^5(\xi)$, respectively. Each is derived through evaluation and factorization and has the form

$$\bar{Q}_g^4(\xi) := \delta_{ik} \bar{Q}_g^4(\xi) e_i \otimes e_k, \quad \bar{Q}_g^5(\xi) := \delta_{ik} \bar{Q}_g^5(\xi) e_i \otimes e_k. \quad (40)$$

The operators for both integration rules are given in Appendix B.

3.4. Volumetric locking

An additional consideration that usually plagues the usage of tetrahedral elements in solid mechanics simulations concerns volumetric locking exhibited by nearly incompressible material response. For the case of modeling metal plasticity, the relevance lies in the isochoric, or volume-preserving, nature of plastic flow. For this reason, special attention is placed towards the interaction of this element with inelastic or plastic material models. Experience of the writers with this topic leads to a modification of the deformation gradient akin to the treatment of the volume-preserving constraint presented in [14]. Here, we seek to replace the volumetric portion of the deformation gradient defined at each integration point within an element with a suitably averaged quantity. This notion is written as follows:

$$\bar{F}^*(\xi) := \left(\frac{\bar{J}^*}{\bar{J}(\xi)} \right)^{\frac{1}{3}} \bar{F}(\xi) \quad (41)$$

where \bar{F}^* is the modified deformation gradient, $\bar{J} = \det \bar{F}$ is the volumetric portion, and \bar{J}^* is the volume-averaged quantity

$$\bar{J}^* := \frac{\int_{\Omega} \bar{J} dV}{\int_{\Omega} dV}. \quad (42)$$

If the edge nodes lie at the midpoint of the edges, we can transform the previous expression into the parametric domain and find

$$\bar{J}^* = \frac{\int_{\Omega_{\xi}} \bar{J} J_{\xi} dV_{\xi}}{\int_{\Omega_{\xi}} J_{\xi} dV_{\xi}} = 6 \int_{\Omega_{\xi}} \bar{J} dV_{\xi}. \quad (43)$$

This simplification is possible because J_{ξ} is constant. As always, the integral requires the values of \bar{J} at the integration points. We note that for the four-point integration rule, \bar{J}^* is merely the arithmetic average of the integration point values. In a variational setting, the volume average (42) also leads to the volume average for the pressure

$$\bar{p}^* := \frac{1}{V_{\Omega}} \int_{\Omega} \text{tr} \frac{\partial A(\bar{F}^*)}{\partial \bar{b}^*} dV \quad (44)$$

where $V_{\Omega} := \int_{\Omega} dV$ and $\bar{b}^* := \bar{F}^*(\bar{F}^*)^T$. We remark that for models with decoupled hyperelastic energy density, the construction of \bar{J}^* already results in a constant pressure formulation, and therefore, there is no need to perform the volume average (44). Also note that volume averaging \bar{J} and \bar{p} is equivalent to projecting them onto a C^{-1} discontinuous constant space.

The volume-averaged formulation (\bar{F}^*, \bar{J}^*) for the composite tetrahedral element renders the displacements to a C^0 continuous piecewise linear space, gradients to a C^{-1} discontinuous linear space, and Jacobians and pressures to a C^{-1} discontinuous constant space.

The numerical results presented later investigate the ramifications of the chosen spaces as we seek to contrast the standard formulation (\bar{F}, \bar{J}) with the volume-averaged formulation (\bar{F}^*, \bar{J}^*) .

4. NUMERICAL RESULTS

The objective of this section is to illustrate the behavior of the preceding element in the context of numerical simulation. To this end, the element is subjected to a patch test to demonstrate the ability of the formulation to capture a constant field. Cook's membrane will be employed to illustrate convergence and the effectiveness of the volume-averaged formulation in the compressible and nearly-incompressible regime. Lastly, we simulate large deformation-necking behavior to explore the ability of the formulation to capture inelastic material response. All the meshes employed in this section were generated with Cubit <http://cubit.sandia.gov> (2015) using the condition number smoother to increase tetrahedral element quality. Simulations were performed with the Sierra/SolidMechanics finite element code [15].

4.1. Patch test

As a step in verifying that the tetrahedral finite element can reproduce a constant deformation gradient field, we construct a parametrized displacement field with coefficients A_i as a function of reference coordinates x , y , and z as follows:

$$u(x, y, z) := \begin{Bmatrix} A_0x + A_1y + A_2z + A_3(xy + xz + yz) \\ A_4x + A_5y + A_6z + A_7(xy + xz + yz) \\ A_8x + A_9y + A_{10}z + A_{11}(xy + xz + yz) \end{Bmatrix}. \quad (45)$$

A general expression for the deformation gradient associated with this prescribed displacement field can be obtained by explicit differentiation with respect to the coordinates as follows:

$$F(x, y, z) = \begin{Bmatrix} 1 + A_0 + A_3(y + z) & A_1 + A_3(x + z) & A_2 + A_3(x + y) \\ A_4 + A_7(y + z) & 1 + A_5 + A_7(x + z) & A_6 + A_7(x + y) \\ A_8 + A_{11}(y + z) & A_9 + A_{11}(x + z) & 1 + A_{10} + A_{11}(x + y) \end{Bmatrix}. \quad (46)$$

The coefficients A_i in (45) can be chosen to induce a constant deformation gradient throughout a domain, and a choice of suitable values is shown in Table III. Note that the coefficients corresponding to the higher-order terms, A_3 , A_7 , and A_{11} are set to zero to achieve the desired constant deformation gradient state. The analytic deformation gradient that arises from the choice of coefficients and applied displacements is shown in (47), and thus, both the values of the deformation gradient and the variation of the deformation gradient throughout a domain can be tested to verify the accuracy of the element.

$$F(x, y, z) = \begin{pmatrix} 1.010 & 0.020 & 0.030 \\ 0.005 & 1.015 & 0.025 \\ 0.015 & 0.025 & 1.035 \end{pmatrix} \quad (47)$$

A cubic domain is discretized, and the aforementioned displacement field is prescribed. External and internal views of the mesh, which consists of 30 composite elements and 61 nodes, are shown in Figure 2.

Table III. Coefficients for the prescribed displacement $u(x, y, z)$ (45) that produce a constant deformation gradient $F(x, y, z)$.

i	0	1	2	3	4	5	6	7	8	9	10	11
$A_i \times 10^3$	10	20	30	0	5	15	25	0	15	25	35	0

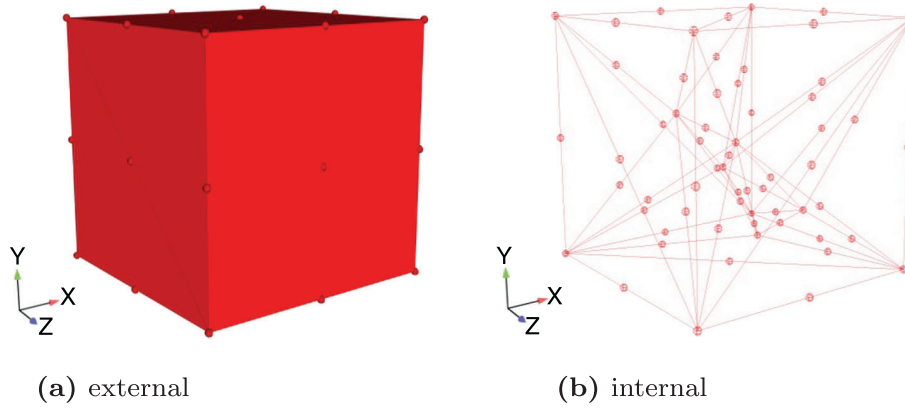


Figure 2. Mesh for the composite tetrahedral patch test, external and internal views.

Table IV. Maximum and average errors in reproducing the analytic deformation gradient (47) for the patch test. The results shown are for the volume-averaged formulation (\bar{F}^* , \bar{J}^*). Results for the standard formulation (\bar{F} , \bar{J}) (not shown) are very similar.

Component ij	Maximum error $e_{ij}^{\max} = F_{ij}^{\max} - F_{ij}^{\min} $	Average error $e_{ij}^{\text{ave}} = F_{ij}^{\text{ave}} - F_{ij}(x, y, z) $
00	1.55431×10^{-15}	1.99840×10^{-15}
01	1.89779×10^{-15}	6.93889×10^{-18}
02	1.13798×10^{-15}	2.42861×10^{-17}
10	6.67001×10^{-16}	1.30104×10^{-17}
11	8.88178×10^{-16}	4.44089×10^{-16}
12	1.09981×10^{-15}	3.46945×10^{-18}
20	1.29063×10^{-15}	2.60209×10^{-17}
21	1.38084×10^{-15}	2.42861×10^{-17}
22	8.88178×10^{-16}	2.22045×10^{-15}

In order to quantify the ability of the element to reproduce the constant field, we compute for each component of $F(x, y, z)$ the maximum and minimum values F_{ij}^{\max} and F_{ij}^{\min} over the domain. Then a measure of field variation, defined as an error, can be constructed as the difference between the extremum for each component, $e_{ij}^{\max} = |F_{ij}^{\max} - F_{ij}^{\min}|$. Table IV shows that the maximum error is sufficiently small, that is, to within machine precision, such that we can conclude that the element is able to accurately reproduce a constant deformation gradient field. Additionally, with this result in hand, we compute F_{ij}^{ave} as the average of each component over the domain and then define the average error as the deviation of the averaged computed deformation gradient components to the analytic components in (47), $e_{ij}^{\text{ave}} = |F_{ij}^{\text{ave}} - F_{ij}(x, y, z)|$. Table IV shows that the error in the values of the deformation gradient components is also sufficiently small.

4.2. Cook's membrane problem

In the spirit of prior works on element technology, we investigate Cook's membrane for compressible and nearly-incompressible deformations. Initial studies in the compressible regime focus on the standard formulation (\bar{F} , \bar{J}) of the three-field Hu–Washizu functional, which results in linear projections for the deformation gradient \bar{F} and the first Piola–Kirchhoff stress \bar{P} . We then move to the nearly-incompressible regime and examine the volume-averaged formulation (\bar{F}^* , \bar{J}^*), which contains volume averages for both the Jacobian \bar{J}^* and the the pressure \bar{p}^* . For the nearly-incompressible regime, displacements belong to a C^0 continuous piecewise linear space; gradients belong to a C^{-1} discontinuous linear space, and Jacobians belong to a C^{-1} discontinuous constant space.

The schematic for the Cook's membrane benchmark is illustrated in Figure 3. A typical mesh for the analysis with an element size of $h = 2$ is adjacent to the schematic. The membrane is loaded with a traction and simulated for a single load step. The hyperelastic model employed for the analysis is a decoupled Neo-Hookean model with a Young's modulus $E = 1000$ and a Poisson's ratio $\nu = 0.25$ or $\nu = 0.49999$. A traction of 1 was applied in one load step. All the simulations in this section were performed in plane strain; therefore, only the upper surface of the finite element model is displayed. The model thickness (in X_3) scales with the mesh size h such that each model is one-element thick and has relatively uniform aspect ratios. The composite tetrahedral element was integrated with four integration points.

Results for the standard formulation subjected to the compressible regime are illustrated in Figure 4. The pressure field converges with increasing refinement. Element sizes of 8, 4, 2, 1, $\frac{1}{2}$, $\frac{1}{4}$, and $\frac{1}{8}$ were employed. We elect to consider that an element size $h = \frac{1}{8}$ to be the converged reference solution. To ease interpretation and avoid the display of multiple integration points, we volume average the pressure within each element for output. We denote this volume-averaged pressure for output as p_0 . The output pressure is normalized by the peak output pressure in the reference solution $\max(p^{\text{ref}}) \approx 2.0$. The pressure is bounded in tension and unbounded (singular) in compression; therefore, we choose a normalized pressure span $p_0 \in [-1, 1]$. Integration point values for the Jacobian \bar{J} and the pressure \bar{p} may be the result of highly nonlinear fields, but the variation of $p_0 / \max(p^{\text{ref}})$, however, is smooth and converges with mesh refinement.

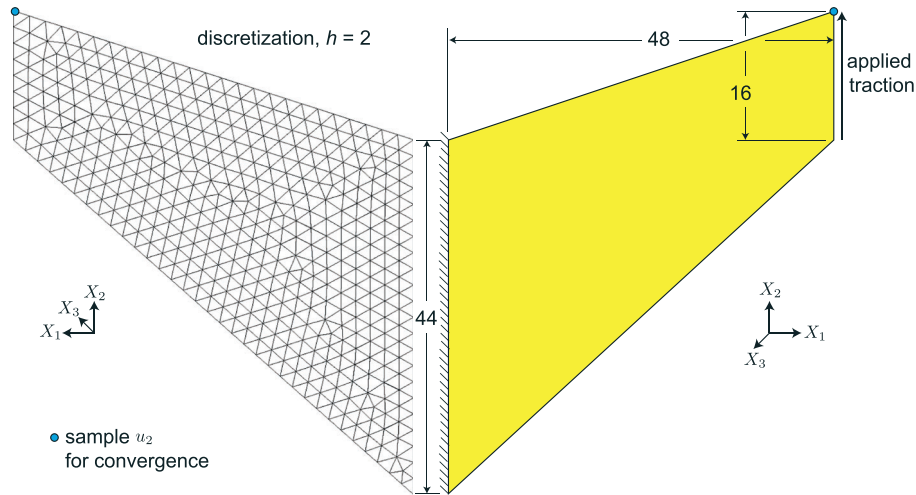


Figure 3. Schematic of Cook's membrane indicating a fixed root and tractions applied to a surface of length 16. The upper surface of a sample discretization with an element size of $h = 2$ is mirrored for the reader.

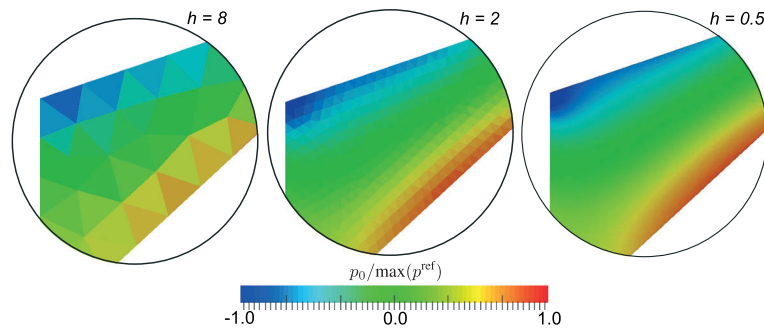


Figure 4. Converging pressure field with increasing refinement for the standard formulation (\bar{F}, \bar{J}) in the compression regime ($\nu = 0.25$). A volume-averaged pressure p_0 within each element is calculated for output and normalized by the peak pressure $\max(p^{\text{ref}})$ in the converged reference solution ($h = \frac{1}{8}$).

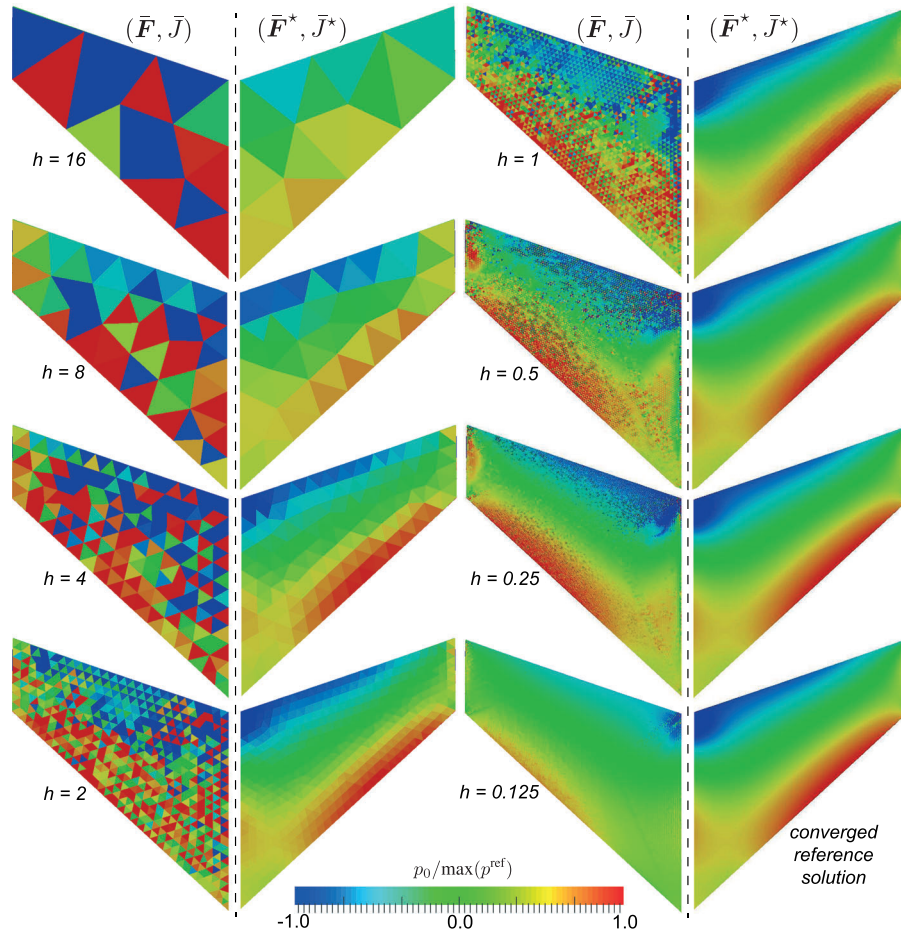


Figure 5. Contrasting the standard formulation (\bar{F}, \bar{J}) and volume-averaged formulation (\bar{F}^*, \bar{J}^*) for nearly-incompressible deformations ($\nu = 0.49999$). For the standard formulation, the normalized pressure field $p_0 / \max(p^{\text{ref}})$ is highly oscillatory and non-convergent. By contrast, the normalized pressure that results from volume-averaged formulation is both smooth and convergent.

After illustrating convergence for the standard formulation for compressible hyperelasticity, we now consider the nearly-incompressible regime. Results for both the standard formulation (\bar{F}, \bar{J}) and the volume-averaged formulation (\bar{F}^*, \bar{J}^*) are shown in Figure 5. The differences in the formulations are striking. For nearly incompressible deformations, the standard formulation locks. The resulting output pressure fields are highly oscillatory and non-convergent. Both the character and values of the pressure field vary with each mesh size. By contrast, subsequent refinements in the mesh size illustrate that the volume-averaged formulation is both smooth and convergent. Even coarse meshes ($h = 8$, $h = 4$) still capture the pressure field. For the volume-averaged formulation, we can identify an equivalence between the output pressure p_0 and the pressure \bar{p}^* defined in (44) that is inherent to this formulation.

In addition to examining the pressure for compressible ($\nu = 0.25$) and nearly incompressible ($\nu = 0.49999$) deformations, we also illustrate the convergence of the maximum nodal displacement in the displacement field for the standard and volume-averaged formulations. The location, shown in Figure 3, is sampled for each mesh size u_2^h and then normalized by the converged reference solution u_2^{ref} . Solutions for both formulations are plotted in Figure 6. Rather than plot the element size, we represent convergence through the number of elements N along the boundary of length 16 (short edge), which supports the traction boundary condition. Simulations with 2, 4, 8, 16, 32, and 64 elements along the edge are illustrated. We note that the converged reference solu-

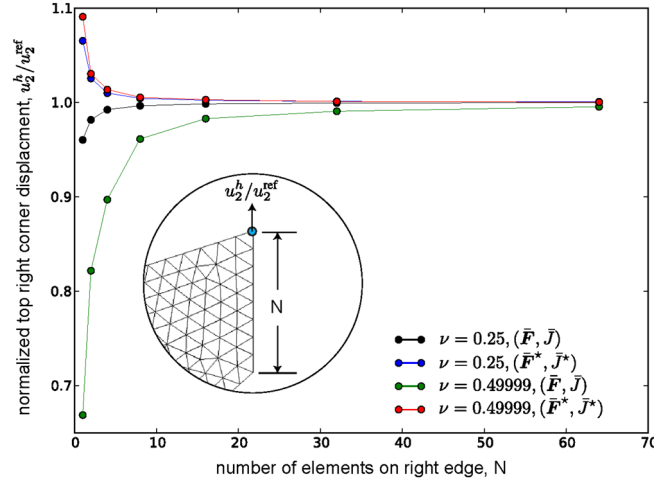


Figure 6. Convergence of the normalized maximum displacement for compressible and nearly incompressible deformations. The maximum displacement u_2^h for each element size h is normalized by the reference solution u_2^{ref} . Although the standard formulation (\bar{F}, \bar{J}) converges in the compressible regime, locking prevents convergence in the nearly incompressible regime. By contrast, the volume-averaged formulation (\bar{F}^*, \bar{J}^*) converges for both regimes.

tion has 128 elements along the short edge. Given the convergent pressure fields noted in Figure 4 and Figure 5, we consider the standard formulation (\bar{F}, \bar{J}) and the volume-averaged formulation (\bar{F}^*, \bar{J}^*) to be the reference solutions for compressible and nearly-incompressible deformations, respectively. Confirming the results of Figure 4, the standard formulation (\bar{F}, \bar{J}) converges in the compressible regime with increasing N . The volume-averaged formulation also converges in the compressible regime with increasing N . The path to convergence in the compressible regime differs in that the standard formulation is stiff while the volume-averaged formulation is compliant. In the nearly incompressible regime, the standard formulation displays significant errors for coarser discretizations and does not converge to the reference solution with increasing N . This result confirms the observed locking noted in Figure 5. The volume-averaged formulation (\bar{F}^*, \bar{J}^*) converges in the normalized displacement with increasing N . As in the compressible case, the volume-averaged formulation for the nearly incompressible case converges from a compliant solution with increasing N . These simplified solutions with hyperelastic models illustrate the importance of the volume-averaged formulation for nearly incompressible deformations. In the next section, we will confirm the need for (\bar{F}^*, \bar{J}^*) in the simulation of large, plastic deformations.

4.3. Large deformation plasticity

To test the element in a regime where tetrahedral elements typically perform poorly, the composite tetrahedron is exercised in a large deformation-necking scenario. The purpose of this exercise is to contrast the standard formulation (\bar{F}, \bar{J}) with the volume-averaged formulation (\bar{F}^*, \bar{J}^*) discussed in previous sections. The large deformation constitutive model employed in the simulation is J_2 plasticity extended to the finite deformation regime with a user-defined hardening law as described in [15]. It is well known that the nature of this model is to generate isochoric motions during plastic flow, potentially leading to volumetric locking in finite element simulations. The hardening behavior of the model obeys the following rate independent law as a function of the equivalent plastic strain ϵ_p

$$\sigma_y = \left[Y + \frac{H}{R_d} (1 - e^{-R_d \epsilon_p}) \right]. \quad (48)$$

Here, Y is the initial yield strength, H is the hardening modulus, and R_d is a recovery modulus. The values for the parameters can be found in Table V. The problem in question is the tensile loading of a rectangular bar that includes various geometric features. Figure 7 shows the undeformed and

Table V. Material properties for the finite-deformation J_2 plasticity model used in the necking simulation.

E	200.0 GPa
ν	0.2490
Y	354.1 MPa
H	2.225 GPa
R_d	1.864

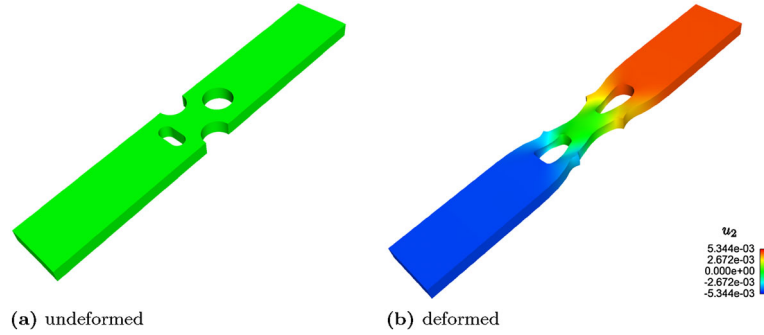


Figure 7. Depiction of the geometry and contours of displacement for the large deformation-necking simulation in both undeformed and deformed configurations.

Table VI. Mesh statistics for the two large deformation problem refinements.

Mesh	$h[\mu\text{m}]$	N_{nodes}	N_{elements}
1	152	453,689	316,505
2	102	1,376,896	991,201

h is the uniform mesh size prescribed in the area of interest, N_{nodes} is the total number of nodes, and N_{elements} is the total number of elements in the model.

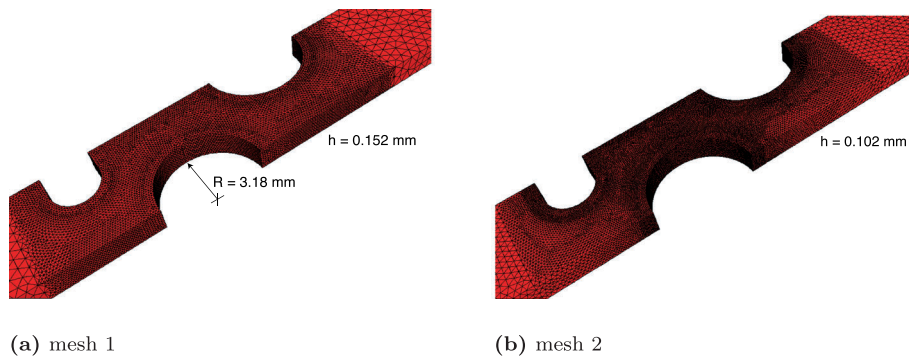


Figure 8. Quarter symmetry zoomed-in view of the geometric-feature rich tensile specimen showing the composite tetrahedron discretization used in the necking study.

deformed configurations of the bar. The purpose of this geometry is to create competing regions of localized deformation, for example, necking, such that the final deformed geometry cannot be known from inspection of the undeformed configuration.

Two finite element models are compared, with relevant mesh sizes and numbers of entities reported in Table VI. The mesh sizes reported are the uniform target element dimension in the areas of interest, adjacent to the geometric features of the specimen. Away from the area of interest, a coarser mesh was used. Automatic meshing algorithms were used to generate the discretization, fol-

lowed by smoothing algorithms to obtain a minimum element quality. Close-up views of the meshes used in this study are shown in Figure 8. Symmetry is exploited in the system, such that only a quarter of the geometry is actually simulated. The boundary conditions consist of equal and opposite prescribed displacement in the X_2 direction at the edges of the domain and appropriate kinematic boundary conditions along the planes of symmetry. The entire geometry is constructed in each of the following plots for clarity in visualizing the physical domain and the fields.

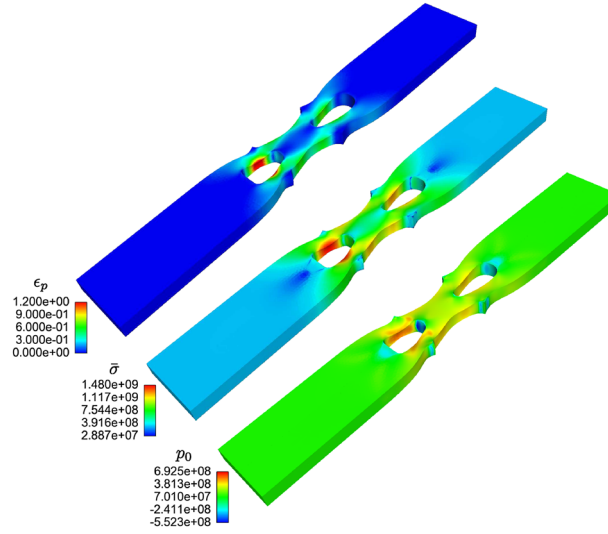


Figure 9. Contours of the equivalent plastic strain ϵ_p , von Mises stress $\bar{\sigma}$, and pressure p_0 fields for Mesh 1 and the volume-averaged formulation (\bar{F}^* , \bar{J}^*). The contours of the field are sufficiently smooth to suggest that the element formulation can adequately capture the gradients and response in this large deformation regime.

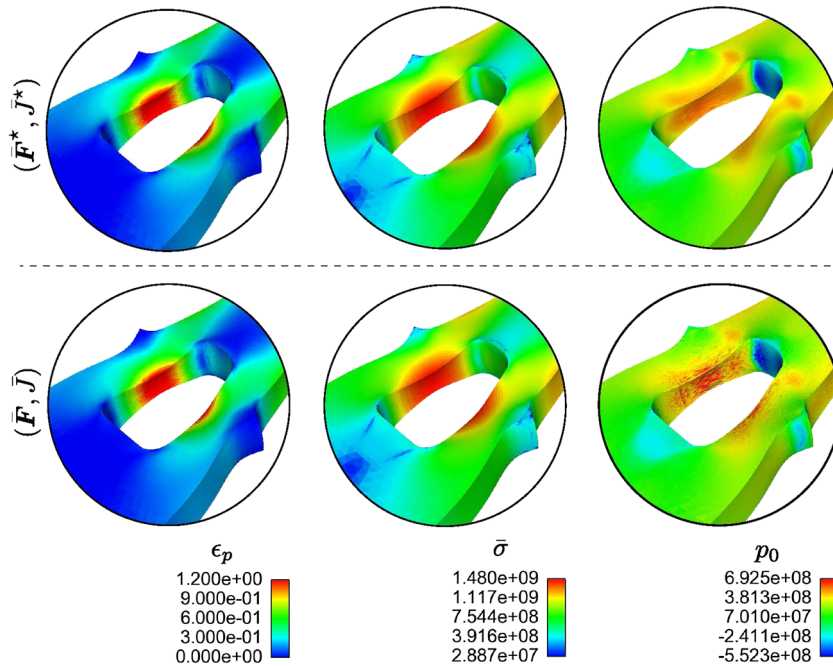


Figure 10. Comparison of the equivalent plastic strain ϵ_p , von Mises stress $\bar{\sigma}$, and pressure p_0 using the standard formulation (\bar{F} , \bar{J}) and the volume-averaged formulation (\bar{F}^* , \bar{J}^*). The pressure field is markedly smoother for the volume-averaged formulation, and the comparison clearly illustrates the benefit of the volume-averaging procedure.

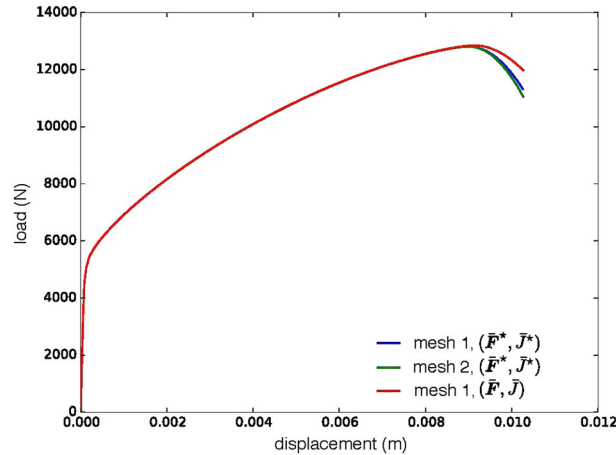


Figure 11. Comparison of the load versus displacement curves for the large deformation-necking response for the standard formulation (\bar{F}, \bar{J}) and the volume-averaged formulation (\bar{F}^*, \bar{J}^*) . Pressure oscillations that arise in the standard formulation produce a stiffer response, as evident in the red curve. The two meshes studied show that the volume-averaged formulation is reasonably resolved.

To observe the resultant fields in the deformed bar, Figure 9 shows contours of equivalent plastic strain ϵ_p , von Mises stress $\bar{\sigma}$, and pressure p_0 , respectively. These field contours show the local variation of the general deformation and stress state. In particular, there are multiple regions of the bar experiencing necking, the most intense being in the lower geometric feature. Evidently, the formulation is capable of resolving the gradients in the stress and strain fields for the highly nonlinear and inelastic deformation.

In Figure 10, a comparison is made for the fields with and without the treatment for volumetric locking. In the plots of equivalent plastic strain and von Mises stress, the fields are nearly identical. However, in the case of the pressure, the volume-averaging procedure improves the smoothness of the field significantly as compared with the unmodified pressure field. This is consistent with the nearly incompressible Cook's membrane results and further proves the value of the volume-averaged formulation.

Figure 11 displays the global load versus displacement curves extracted from the simulation. It is clear that the volume averaging procedure has an effect on the compliance of the system in the post-necking regime. The manifestation of spurious pressure fields during isochoric motion tends to stiffen the system, explaining the discrepancy seen in Figure 10. The two meshes studied show that the volume-averaged formulation is reasonably resolved.

5. DISCUSSION

The implications of having a usable tetrahedral element for solid mechanics are significant for the design and analysis of structures. The time spent meshing complicated geometries is significantly reduced, as compared with producing hexahedral meshes, because of robust automatic tetrahedral meshing technology. The same algorithms employed for automatic remeshing, coupled with algorithms and methodologies for the transfer of the material state between discretizations [16], facilitate the study of accurate and robust adaptivity algorithms suitable for very large deformation behavior.

A promising formulation is the tetrahedral composite element proposed in [4]. The authors advance this element in the context of simulations that involve dynamics, contact, and isochoric deformations. Our initial work with this element formulation, however, revealed potential issues in the integration scheme and its performance under isochoric deformations.

Consequently, we reformulated the element exploiting the underlying simplicial structure of the finite element topology to obtain analytic gradient and projection operators in parametric space. We achieve analytic operators despite the complexity of the variational formulation and the inherent projection operations into the assumed linear spaces for the deformation gradient and stress. This

development crucially allows for the usage of standard Gauss–Legendre numerical integration rules, improving element accuracy and also significantly simplifying the element implementation. In fact, we find that the four-point rule is sufficient for full integration (*cf.* [4]).

A consequence of our parametric formalism is the requirement for edge nodes to be located at the midpoint of each edge. This is clearly the most accurate simulation scenario. We do, however, permit edge nodes to deviate from their ideal positions, for example, to represent curved surface geometries. For these cases, appropriate configurations and mappings are generated that allow for the consistent utilization of the analytic operators, as described in Appendix 6.

To address isochoric deformations, the present work introduces volume averaging operations on the determinant of the deformation gradient and the pressure. Employing this strategy involves modifications to the deformation gradient and stress tensors at each integration point to account for the volume-averaged quantities. The motivation for this volume-averaged formulation (\bar{F}^* , \bar{J}^*) stems from the ideas presented in [14] and others.

For the nearly incompressible cases explored in Section 4, the convergence of the pressure field is strongly affected by the volume averaging procedures for \bar{J} and \bar{p} . In fact, it appears that the pressure field does not converge if the volumetric fields are left in the original spaces of the standard formulation (\bar{F} , \bar{J}). This behavior has implications for other important phenomena, such as stress wave propagation, pressure dependent plasticity models, inelastic damage models that depend on pressure, and incorporating equation of state models to capture shock behavior. In each of these cases, accurate results hinge on the pressure field. Therefore, spurious oscillatory behavior leads to inaccurate and sometimes disastrous results.

In the present work, we have provided all the necessary details required to implement the element in a quasi-static solid mechanics finite element code. In addition, source code is available through the open source Trilinos and Albany projects at <http://www.trilinos.org> and <https://github.com/gahansen/Albany>.

The next steps for this research are investigating the performance and usability of the reformulated composite tetrahedron. We seek to quantify the performance of the composite tetrahedron when compared with other tetrahedral and hexahedral elements. In addition, the application of the composite tetrahedron element to coupled thermomechanical problems will contrast the element quality needed for thermal and mechanical boundary value problems. Near-term efforts include adaptive remeshing and mapping of internal variables and dynamic behavior under both explicit and implicit time integrators.

6. CONCLUSION

This work illustrates the reformulated 10-node composite tetrahedral element for solid mechanics. Our contributions include the following:

- (1) Clear presentation of the finite element formulation, which derives from the three-field Hu–Washizu functional and results in C^{-1} linear projections of F and P , which we term the standard formulation (\bar{F} , \bar{J}). We also linearize the residual and present a direct form of the B-bar gradient operator.
- (2) Detailed description of the sub-tetrahedral domains (E_0, \dots, E_{11}) and the shape functions (N_0, \dots, N_9) governing the composite tetrahedral element.
- (3) Development of an exact, analytical, parametric gradient operator $\bar{\mathcal{L}}_a(\xi)$ that projects and interpolates the parametric gradients of the 12 sub-tetrahedra into a C^{-1} linear space for arbitrary cubature schemes. The composition of operators via the chain rule forms the global gradient operator $\bar{\mathcal{B}}_a(\xi)$.
- (4) Development of analytical projection operators for four-point $\bar{Q}_g^4(\xi)$ and five-point $\bar{Q}_g^5(\xi)$ integration rules. The resulting operator for the four-point rule is the identity, $\bar{P}(\xi_g) = P(\xi_g)$.
- (5) Development of an alternative volume-averaged formulation (\bar{F}^* , \bar{J}^*) to mitigate volumetric locking. For this alternative formulation, displacements u belong to a C^0 continuous piecewise linear space; gradients \bar{F}^* belong to a C^{-1} discontinuous linear space, and Jacobians \bar{J}^* and pressure \bar{p}^* belong to a C^{-1} discontinuous constant space.

- (6) Verification that both the standard formulation (\bar{F}, \bar{J}) and the volume-averaged formulation (\bar{F}^*, \bar{J}^*) pass the patch test.
- (7) A series of simulations of Cook's membrane in the compressible regime that demonstrate convergence for the standard formulation. Additional simulations in the nearly incompressible regime, however, illustrate the need for the alternative, volume-averaged formulation to avoid pressure oscillations. The alternative formulation converges in the nearly incompressible regime.
- (8) The applicability of the 10-node composite tetrahedral element for large deformation plasticity. Large plastic strains are resolved in the necking of a complex geometry. The alternative, volume-averaged formulation results in pressure fields that are free of spurious oscillations.
- (9) Explicit expressions for matrix gradient and projection operators, consistent and lumped mass matrices, and a kinematic extension for meshes with edge nodes not located at the midpoints. These details are included in the appendices for completeness and replicability.

APPENDIX A: GRADIENT OPERATOR

We begin by re-writing the deformation gradient in indicial notation through the parametric gradient operator shown in (36)

$$\bar{F}_{iJ}(X) = \bar{\mathcal{L}}_{a;ilk}(\xi) [\bar{\mathcal{L}}_{b;JlM}(\xi) X_{b;M}]^{-1} x_{a;k} \quad (\text{A.1})$$

and note that the parametric gradient operator expressed in (33) acting on the current coordinates yields parametric derivatives

$$\frac{\partial x_i}{\partial \xi_l} = \bar{\mathcal{L}}_{a;ilk}(\xi) x_{a;k} = \lambda_\alpha(\xi) (M_{\alpha\beta})^{-1} \sum_{S=0}^{11} \frac{\partial N_a}{\partial \xi_l} \int_{E_S} \lambda_\beta(\xi) dV_\xi x_{a;i}. \quad (\text{A.2})$$

These expressions can be simplified through a matrix operator $\bar{L}_{la}(\xi)$ of the form

$$\frac{\partial x_i}{\partial \xi_l} = [\bar{L}_{la}(\xi) x_{ai}]^T = x_{ia} \bar{L}_{al}(\xi). \quad (\text{A.3})$$

For completeness, we express the linear shape functions λ_α for the parent tetrahedral element Ω_ξ spanning $\xi_1 \in [0, 1]$, $\xi_2 \in [0, 1]$, $\xi_3 \in [0, 1]$, and $\xi_1 + \xi_2 + \xi_3 \in [0, 1]$

$$\begin{aligned} \lambda_0(\xi) &:= \xi_0, & \lambda_1(\xi) &:= \xi_1, \\ \lambda_2(\xi) &:= \xi_2, & \lambda_3(\xi) &:= \xi_3 \end{aligned} \quad (\text{A.4})$$

and remind the reader that $\xi := (\xi_1, \xi_2, \xi_3)$ and $\xi_0 := 1 - \xi_1 - \xi_2 - \xi_3$. If we construct a row vector for the parent shape functions $\lambda_{1 \times 4}$ and define the integrand of (32) to be $(\lambda_{1 \times 4})^T \lambda_{1 \times 4}$, we find

$$M_{\alpha\beta} \equiv M_{4 \times 4} = 24 \begin{pmatrix} 4 & -1 & -1 & -1 \\ -1 & 4 & -1 & -1 \\ -1 & -1 & 4 & -1 \\ -1 & -1 & -1 & 4 \end{pmatrix}. \quad (\text{A.5})$$

Given matrix expressions for the parent shape functions and the projection matrix, we can re-express \bar{L}_{al} as follows:

$$\bar{L}_{al}(\xi) = \lambda_{1 \times 4} (M_{4 \times 4})^{-1} \sum_{S=0}^{11} \frac{\partial N_a}{\partial \xi_l} \int_{E_S} (\lambda_{1 \times 4})^T dV_\xi \quad (\text{A.6})$$

and note that each component $\bar{L}_{la}(\xi)$ stems from the projection of discontinuous derivatives of a given shape function N_a with respect to a parametric coordinate ξ_l into a linear space. The

derivatives and integrals can be evaluated analytically for each sub-tetrahedra E_S . Projections and interpolations then yield the parametric gradient operator as follows:

$$\begin{aligned} \bar{L}_{al}(\xi) &\equiv \bar{L}_{10 \times 3} \\ &= \frac{1}{24} \begin{pmatrix} 9 - 60\xi_0 & 9 - 60\xi_0 & 9 - 60\xi_0 \\ -9 + 60\xi_1 & 0 & 0 \\ 0 & -9 + 60\xi_2 & 0 \\ 0 & 0 & -9 + 60\xi_3 \\ 70(\xi_0 - \xi_1) & 2(-4 - 35\xi_1 + 5\xi_2 + 10\xi_3) & 2(-4 - 35\xi_1 + 10\xi_2 + 5\xi_3) \\ 2(-1 + 5\xi_1 + 40\xi_2 - 5\xi_3) & 2(-1 + 40\xi_1 + 5\xi_2 - 5\xi_3) & 10(\xi_0 - \xi_3) \\ 2(-4 + 5\xi_1 - 35\xi_2 + 10\xi_3) & 70(\xi_0 - \xi_2) & 2(-4 + 10\xi_1 - 35\xi_2 + 5\xi_3) \\ 2(-4 + 5\xi_1 + 10\xi_2 - 35\xi_3) & 2(-4 + 10\xi_1 + 5\xi_2 - 35\xi_3) & 70(\xi_0 - \xi_3) \\ 2(-1 + 5\xi_1 - 5\xi_2 + 40\xi_3) & 10(\xi_0 - \xi_2) & 2(-1 + 40\xi_1 - 5\xi_2 + 5\xi_3) \\ 10(\xi_0 - \xi_1) & 2(-1 - 5\xi_1 + 5\xi_2 + 40\xi_3) & 2(-1 - 5\xi_1 + 40\xi_2 + 5\xi_3) \end{pmatrix}. \end{aligned} \quad (\text{A.7})$$

The expression shown in (A.7) is novel in that it is exact and therefore independent of any numerical integration scheme. Through the chain rule, we arrive at the matrix gradient operator

$$\bar{B}_{aJ}(\xi) = \bar{L}_{al}(\xi) [X_{Jb} \bar{L}_{bl}(\xi)]^{-1} \quad (\text{A.8})$$

and

$$\bar{F}_{iJ}(\xi) = x_{ia} \bar{B}_{aJ}(\xi). \quad (\text{A.9})$$

APPENDIX B: PROJECTION OPERATORS

If we employ the process noted in Section 3.3, we can obtain the projection operators $\bar{Q}_g^4(\xi)$ and $\bar{Q}_g^5(\xi)$ for the four-point and five-point integration rules, respectively. For the four-point rule, we have

$$\begin{aligned} \bar{Q}_0^4(\xi) &:= \frac{1}{4} (1 - \sqrt{5} + 4\sqrt{5}\xi_0), & \bar{Q}_1^4(\xi) &:= \frac{1}{4} (1 - \sqrt{5} + 4\sqrt{5}\xi_1), \\ \bar{Q}_2^4(\xi) &:= \frac{1}{4} (1 - \sqrt{5} + 4\sqrt{5}\xi_2), & \bar{Q}_3^4(\xi) &:= \frac{1}{4} (1 - \sqrt{5} + 4\sqrt{5}\xi_3), \end{aligned} \quad (\text{B.1})$$

corresponding to the integration point locations

$$\begin{aligned} \xi_0^4 &:= \frac{1}{20} (5 - \sqrt{5}, 5 - \sqrt{5}, 5 - \sqrt{5}), & \xi_1^4 &:= \frac{1}{20} (5 + 3\sqrt{5}, 5 - \sqrt{5}, 5 - \sqrt{5}), \\ \xi_2^4 &:= \frac{1}{20} (5 - \sqrt{5}, 5 + 3\sqrt{5}, 5 - \sqrt{5}), & \xi_3^4 &:= \frac{1}{20} (5 - \sqrt{5}, 5 - \sqrt{5}, 5 + 3\sqrt{5}). \end{aligned} \quad (\text{B.2})$$

All the weights for the four-point rule are $\frac{1}{24}$. For the five-point rule, we have

$$\begin{aligned} \bar{Q}_0^5(\xi) &:= -\frac{4}{5}, \\ \bar{Q}_1^5(\xi) &:= 3(\xi_0 - \frac{1}{10}), & \bar{Q}_2^5(\xi) &:= 3(\xi_3 - \frac{1}{10}), \\ \bar{Q}_3^5(\xi) &:= 3(\xi_2 - \frac{1}{10}), & \bar{Q}_4^5(\xi) &:= 3(\xi_1 - \frac{1}{10}), \end{aligned} \quad (\text{B.3})$$

corresponding to the integration point locations

$$\begin{aligned} \xi_0^5 &:= (\frac{1}{4}, \frac{1}{4}, \frac{1}{4}), \\ \xi_1^5 &:= (\frac{1}{6}, \frac{1}{6}, \frac{1}{6}), & \xi_2^5 &:= (\frac{1}{6}, \frac{1}{6}, \frac{1}{2}), \\ \xi_3^5 &:= (\frac{1}{6}, \frac{1}{2}, \frac{1}{6}), & \xi_4^5 &:= (\frac{1}{2}, \frac{1}{6}, \frac{1}{6}). \end{aligned} \quad (\text{B.4})$$

The corresponding weights to ξ_0^5 , ξ_1^5 , ξ_2^5 , ξ_3^5 , and ξ_4^5 are $-\frac{2}{15}$, $\frac{3}{40}$, $\frac{3}{40}$, $\frac{3}{40}$, and $\frac{3}{40}$, respectively. We note that in both cases, the projection operators sum to one. In addition, for the case of four integration points, the projection operator Q_g^4 reduces to the identity I at each integration point ξ_g . In other words, for the four-point integration rule, the intra-element projection yields $\bar{P}(\xi_g) = P(\xi_g)$, and consequently, the projection is not needed for this integration rule as the first Piola–Kirchhoff stress over the parent tetrahedron is already an element of a linear space.

APPENDIX C: CONSISTENT AND LUMPED MASS MATRICES

For completeness, we derive analytic forms for both the consistent and lumped mass matrices. Forming a row vector for the shape functions $N_{10 \times 1}$ expressed in Section 3.1, one can write the element mass matrix as follows:

$$M_{10 \times 10}^c = \int_{\Omega} \rho(X) (N_{10 \times 1})^T N_{10 \times 1} dV \quad (C.1)$$

and remind the reader that the shape functions composing $N_{10 \times 1}$ are effective shape functions that have distributed contributions of N_{10} to the mid-side nodes. To obtain an understanding of how the mass is distributed, we normalize (C.1) by the element mass and find

$$\bar{M}_{10 \times 10}^c = \frac{\int_{\Omega} \rho(X) (N_{10 \times 1})^T N_{10 \times 1} dV}{\int_{\Omega} \rho(X) dV}. \quad (C.2)$$

The normalized mass matrix can be simplified through a mapping to the parametric domain. We again note that if the edge nodes are located at the midpoint, the parametric Jacobian J_{ξ} is constant. For a constant element density, this simplification yields

$$\bar{M}_{10 \times 10}^c = 6 \int_{\Omega_{\xi}} (N_{10 \times 1})^T N_{10 \times 1} dV_{\xi}. \quad (C.3)$$

The element mass matrix can be easily found by merely multiplying the normalized mass matrix by the element mass. Expression (C.3) enables an analytic evaluation of the normalized consistent mass matrix

$$\bar{M}_{10 \times 10}^c = \begin{pmatrix} \frac{1}{80} & 0 & 0 & 0 & \frac{1}{160} & 0 & \frac{1}{160} & \frac{1}{160} & 0 & 0 \\ 0 & \frac{1}{80} & 0 & 0 & \frac{1}{160} & \frac{1}{160} & 0 & 0 & \frac{1}{160} & 0 \\ 0 & 0 & \frac{1}{80} & 0 & 0 & \frac{1}{160} & \frac{1}{160} & 0 & 0 & \frac{1}{160} \\ 0 & 0 & 0 & \frac{1}{80} & 0 & 0 & 0 & \frac{1}{160} & \frac{1}{160} & \frac{1}{160} \\ \frac{1}{160} & \frac{1}{160} & 0 & 0 & \frac{1}{18} & \frac{13}{720} & \frac{13}{720} & \frac{13}{720} & \frac{13}{720} & \frac{1}{180} \\ 0 & \frac{1}{160} & \frac{1}{160} & 0 & \frac{13}{720} & \frac{1}{18} & \frac{13}{720} & \frac{1}{180} & \frac{13}{720} & \frac{13}{720} \\ \frac{1}{160} & 0 & \frac{1}{160} & 0 & \frac{13}{720} & \frac{13}{720} & \frac{1}{18} & \frac{13}{720} & \frac{1}{180} & \frac{13}{720} \\ \frac{1}{160} & 0 & 0 & \frac{1}{160} & \frac{13}{720} & \frac{1}{180} & \frac{13}{720} & \frac{1}{18} & \frac{13}{720} & \frac{13}{720} \\ 0 & \frac{1}{160} & 0 & \frac{1}{160} & \frac{13}{720} & \frac{13}{720} & \frac{1}{180} & \frac{13}{720} & \frac{1}{18} & \frac{13}{720} \\ 0 & 0 & \frac{1}{160} & \frac{1}{160} & \frac{1}{180} & \frac{13}{720} & \frac{13}{720} & \frac{13}{720} & \frac{13}{720} & \frac{1}{18} \end{pmatrix}. \quad (C.4)$$

We note that in contrast to the mass matrix for the four-noded tetrahedron, the composite tetrahedral element does not contain negative off-diagonal entries. All entries are positive. Given the consistent mass matrix, we can construct a lumped mass matrix via the row-sum technique [17]. The resulting normalized, lumped mass matrix is as follows:

$$\bar{M}_{10 \times 10}^1 = \begin{pmatrix} \frac{1}{32} & 0 & 0 & 0 & 0 & 0 & 0 & 0 & 0 & 0 \\ 0 & \frac{1}{32} & 0 & 0 & 0 & 0 & 0 & 0 & 0 & 0 \\ 0 & 0 & \frac{1}{32} & 0 & 0 & 0 & 0 & 0 & 0 & 0 \\ 0 & 0 & 0 & \frac{1}{32} & 0 & 0 & 0 & 0 & 0 & 0 \\ 0 & 0 & 0 & 0 & \frac{7}{48} & 0 & 0 & 0 & 0 & 0 \\ 0 & 0 & 0 & 0 & 0 & \frac{7}{48} & 0 & 0 & 0 & 0 \\ 0 & 0 & 0 & 0 & 0 & 0 & \frac{7}{48} & 0 & 0 & 0 \\ 0 & 0 & 0 & 0 & 0 & 0 & 0 & \frac{7}{48} & 0 & 0 \\ 0 & 0 & 0 & 0 & 0 & 0 & 0 & 0 & \frac{7}{48} & 0 \\ 0 & 0 & 0 & 0 & 0 & 0 & 0 & 0 & 0 & \frac{7}{48} \end{pmatrix}. \quad (C.5)$$

Inspection confirms that the sum of the nodal masses is one. The lumped mass matrix in (C.5) mirrors the expression in [4]. Although we have arrived at the lumped mass matrix rigorously, one can also make geometric arguments for each component of $\bar{M}_{10 \times 10}^1$. As before, we assume that the density of the element is constant. Each sub-tetrahedron connected to a corner node (0, 1, 2, 3) has a sub-volume of $\frac{1}{8}$. Consequently, each corner node has a tributary volume of $\frac{1}{32}$. If we equally allocate the remaining volumes based on symmetry, we find that the tributary volumes for all edge nodes are $\frac{7}{48}$. Although the geometric argument is intuitive, there is an implicit assumption, which ties the reference domain to the parametric domain, and, that is, that all edge nodes (4, 5, 6, 7, 8, 9) must be located at the edge midpoints.

APPENDIX D: EXTENSION TO ARBITRARY EDGE NODES

The simplifications introduced in Section 3.2.1 rely on the edge nodes being located at the midpoints. For this case, the analytical gradient operator illustrated in Appendix A is exact. Small perturbations in the edge nodes through mesh creation and/or smoothing, however, will result in loss of accuracy. We now seek to establish a global gradient operator that operates on edges nodes with an arbitrary location and remains exact. In the spirit of (24), we re-express the chain rule

$$\frac{\partial N_a(X)}{\partial X} = \frac{\partial N_a(X)}{\partial Y} \left[\frac{\partial X}{\partial Y} \right]^{-1} \quad (D.1)$$

where Y are the coordinates of a new reference configuration Ω in which the edge nodes are constructed to be midpoints and X are the coordinates of the possibly arbitrary (i.e., the edge nodes not being midpoints) and un-stressed configuration Ω_X , which stems from the given discretization. The new reference configuration Ω_Y and multiplicative decomposition are illustrated in Figure A.1.

We remind the reader that the constructed configuration Ω with coordinates Y is employed to take advantage of the simplifications derived in Section 3.2.1. Intra-element projections for \bar{F} and \bar{P} are computed (analytically) in the new reference configuration Ω and not the discretized configuration Ω_X . One may view this new reference configuration as an additional parametric system convenient for computation. For edge nodes located at the midpoints, $\partial X / \partial Y = I$. In parallel with (35), we define the deformation gradient for the arbitrary configuration to be

$$\bar{F}(\xi) = \bar{\mathcal{B}}_a(\xi) x_a [\bar{\mathcal{B}}_b(\xi) X_b]^{-1} \quad (D.2)$$

and propose a modified gradient operator

$$\hat{\bar{\mathcal{B}}}_a(\xi) = \bar{\mathcal{B}}_{a;ilk}(\xi) [\bar{\mathcal{B}}_{b;JlM}(\xi) X_{b;M}]^{-1} e_i \otimes E_J \otimes e_k, \quad (D.3)$$

which yields

$$\bar{F}(\xi) = \hat{\bar{\mathcal{B}}}_a(\xi) x_a. \quad (D.4)$$

With the change in the reference configuration, the $\bar{\mathcal{B}}_a(\xi)$ operator yields derivatives with respect to Y and not X . In the spirit of (D.1), we have now defined an additional operator $\hat{\bar{\mathcal{B}}}_a(\xi)$ that yields derivatives with respect to X .

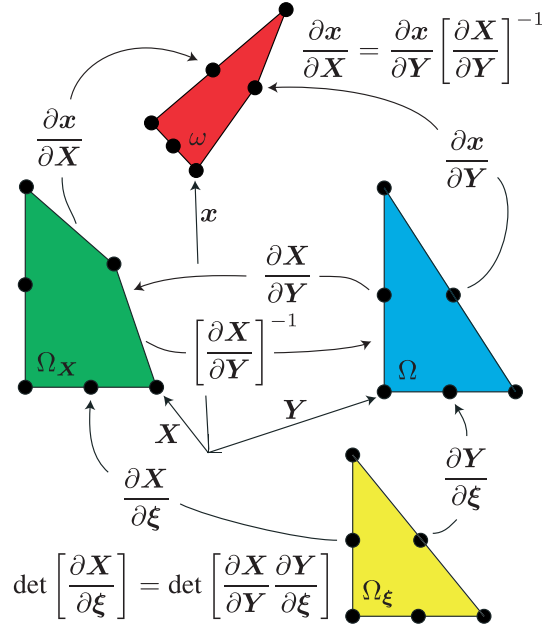


Figure A.1. Requisite mappings for extension to arbitrary edge nodes.

The matrix gradient operator for arbitrary edge nodes directly follows from Appendix A. We redefine the matrix gradient operator expressed in (A.8) as follows:

$$\bar{B}_{aJ}(\xi) = \bar{L}_{aI}(\xi) [Y_{Jb} \bar{L}_{bI}(\xi)]^{-1}. \quad (\text{D.5})$$

The redefined matrix operator $\bar{B}_{aJ}(\xi)$ yields gradients with respect to Y and not X . In the spirit of the chain rule, we can then construct a modified matrix gradient operator as follows:

$$\hat{\bar{B}}_{aJ}(\xi) = \bar{B}_{aK}(\xi) [X_{Jb} \bar{B}_{bK}(\xi)]^{-1}, \quad (\text{D.6})$$

which results in gradients with respect to X

$$\bar{F}_{iJ}(\xi) = x_{ia} \hat{\bar{B}}_{aJ}(\xi) \quad (\text{D.7})$$

for arbitrary edge nodes. In addition to modifying the gradient operator at each integration point, we must also modify the integration scheme to account for the new reference configuration. We define the volume of a single element to be

$$V = \int_{\Omega_X} dV_X \quad (\text{D.8})$$

and push the integration back to the new reference configuration

$$V = \int_{\Omega} \det \left[\frac{\partial X}{\partial Y} \right] dV = \int_{\Omega} J_{X,Y}(\xi) dV \quad (\text{D.9})$$

and ultimately into the parametric coordinate system as follows:

$$V = \int_{\Omega_\xi} J_{X,Y}(\xi) J_\xi dV_\xi. \quad (\text{D.10})$$

Through (D.10), we conclude that the aforementioned mapping of volume elements from the parametric to the discretized configuration $J_{X,\xi}(\xi)$ is equivalent to the composition $J_{X,Y}(\xi) J_\xi$. A

variation of the Jacobian in the parametric domain reflects the fact that the edge nodes are not located at the midpoint. We note that if the gradient of the mapping between Ω and Ω_X is sufficiently heterogeneous, the projection of $\partial X/\partial Y$ into a linear space may not be exact. Consequently, the volume will be approximate. In practice, the mid-edge nodes would potentially deviate from the midpoint on the surface of the body. One would better approximate the geometry through the projection of mid-edge nodes to the surface. Future studies will contrast increases in geometric fidelity with approximations in the gradient operator and the resulting element volume.

The adoption of a new reference configuration also impacts the force calculation. The role of $\bar{\mathbf{B}}_a$ in the computation of nodal forces is illustrated by (17). We note that $\bar{\mathbf{B}}_a$ now derives from Y and not X . The additional operator, $\hat{\mathbf{B}}_a(\xi)$, defined in (D.4), is employed for the kinematics and not the forces. As shown in Figure A.1, we must pull-back the Cauchy stress from the current configuration through $\partial x/\partial Y$ and integrate the forces in the new reference configuration Ω with $\bar{\mathbf{B}}_a$.

ACKNOWLEDGEMENTS

The authors are grateful for the support of our managers and colleagues at Sandia National Laboratories in the development of tetrahedral element technology. We appreciate Brad Boyce's openness to sharing his unique specimen geometry designed for quantifying ductile necking processes. Special thanks to Michael Tupek for his insightful comments regarding the extension of the gradient operator to arbitrarily placed edge nodes and Kendall Pierson for his continued support and patience in the development of a robust higher-order tetrahedral element for the Sierra Solid Mechanics finite element code. Sandia National Laboratories is a multi-program laboratory managed and operated by Sandia Corporation, a wholly owned subsidiary of Lockheed Martin Corporation, for the US Department of Energy's National Nuclear Security Administration under contract DE-AC04-94AL85000.

REFERENCES

1. Danielson KT. Fifteen node tetrahedral elements for explicit methods in nonlinear solid dynamics. *Computer Methods in Applied Mechanics and Engineering* 2014; **272**:160–180.
2. Irving G, Schroeder C, Fedkiw R. Volume conserving finite element Simulations of deformable models. *ACM Transactions on Graphics* 2007; **26**(3):13:1–13:6. ACM SIGGRAPH 2007 Conference, San Diego, CA, AUG 05-09, 2007-2008.
3. Puso MA, Solberg J. A stabilized nodally integrated tetrahedral. *International Journal for Numerical Methods in Engineering* 2006; **67**(6):841–867.
4. Thoutireddy P, Molinari JF, Repetto EA, Ortiz M. Tetrahedral composite finite elements. *International Journal for Numerical Methods in Engineering* 2002; **53**(6):1337–1351.
5. Klaas O, Maniatty AM, Shephard MS. A stabilized mixed finite element method for finite elasticity.: formulation for linear displacement and pressure interpolation. *Computer Methods in Applied Mechanics and Engineering* 1999; **180**(1):65–79.
6. Maniatty AM, Liu Y, Klaas O, Shephard MS. Higher order stabilized finite element method for hyperelastic finite deformation. *Computer Methods in Applied Mechanics and Engineering* 2002; **191**(13):1491–1503.
7. Scovazzi G, Carnes B, Zeng X. A simple, stable, and accurate tetrahedral finite element for transient, nearly incompressible, linear and nonlinear elasticity: A dynamic variational multiscale approach. *International Journal for Numerical Methods in Engineering* 2015.
8. Dohrmann CR, Heinstein MW, Jung J, Key SW, Witkowski WR. Node-based uniform strain elements for three-node triangular and four-node tetrahedral meshes. *International Journal for Numerical Methods in Engineering* 2000; **47**(9):1549–1568.
9. Gee MW, Dohrmann CR, Key SW, Wall WA. A uniform nodal strain tetrahedron with isochoric stabilization. *International Journal for Numerical Methods in Engineering* 2009; **78**(4):429–443.
10. Puso MA, Solberg J. A stabilized nodally integrated tetrahedral. *International Journal for Numerical Methods in Engineering* 2006; **67**(6):841–867.
11. Guo Y, Ortiz M, Belytschko T, Repetto EA. Triangular composite finite elements. *International Journal for Numerical Methods in Engineering* 2000; **47**(1-3):287–316.
12. Preusser T, Rumpf M, Sauter S, Schwen LO. 3D Composite finite elements for elliptic boundary value problems with discontinuous coefficients. *SIAM Journal on Scientific Computing* 2011; **33**(5):2115–2143.
13. de Souza EA, Andrade FM, Owen DRJ. F-bar-based linear triangles and tetrahedra for finite strain analysis of nearly incompressible solids. Part I: formulation and benchmarking. *International Journal for Numerical Methods in Engineering* 2005; **62**(3):353–383.

14. Simo JC, Taylor RL, Pister KS. Variational and projection methods for the volume constraint in finite deformation elasto-plasticity. *Computer Methods in Applied Mechanics and Engineering* 1985; **51**(1-3):177–208.
15. SIERRA Solid Mechanics Team. Sierra/SolidMechanics 4.36 user's guide, SAND Report 2015-2199, Sandia National Laboratories: Albuquerque, NM and Livermore, CA, 2015.
16. Mota A, Sun W, Ostien JT, Foulk JW, Long KN. Lie-group interpolation and variational recovery for internal variables. *Computational Mechanics* 2013; **52**(6):1281–1299.
17. Schreyer HL. Dispersion of semidiscretized and fully discretized systems. In *Numerical Methods for Transient Analysis*, Belytschko T, Hughes TJR (eds): North-Holland, 1983; 267–298.